Supplementary Information for

Magnetotransport evidence for the coexistence of two-dimensional superconductivity and ferromagnetism at (111)-oriented a-$CaZrO_3$/$KTaO_3$ interfaces

Hui Zhang[1‡*], Yinan Xiao[1‡], Qixuan Gao[2‡], Ning Wu[3,4‡], Siyi Zhou[2], Yongchao Wang[2], Mengqin Wang[5,6], Daming Tian[1], Lu Chen[1], Weijian Qi[1], Dongyao Zheng[1], Jine Zhang[1], Furong Han[1], Huaiwen Yang[1], Banggui Liu[5,6], Yuansha Chen[5,6], Fengxia Hu[5,6,7], Baogen Shen[5,6,8], Jirong Sun[5,9*], Weisheng Zhao[1*] and Jinsong Zhang[2,10,11*]

[‡]These authors contributed equally: Hui Zhang, Yinan Xiao, Qixuan Gao, Ning Wu

*Corresponding Authors:
huizh@buaa.edu.cn
jrsun@iphy.ac.cn
wszhao@buaa.edu.cn
jinsongzhang@mail.tsinghua.edu.cn

This file includes:

Notes 1 and 2
Tables S1 to S3
Figs. S1 to S21

Note 1: Back gating effect of a-CZO/KTO(111) sample

We systematically investigated the back gating effect for the a-CZO/KTO(111) sample with n_S=3.8×10^{13} cm^{-2}, which corresponds to the n_S value of the as-grown sample. Fig. S6a presents the temperature dependence of R_S measured under varying gating voltage V_G. When V_G changes from +150 V to -100 V, the normal-state sheet resistance at T=1.2 K ($R_{1.2K}$) increases from 1220.9 to 1863.0 Ω/□, while superconducting transition shifts to higher temperatures. As illustrated in the inset of Fig. S6a, the midpoint T_C, derived from the R_S-T curves, increases monotonically as V_G decreases. To further characterize the tunable effects, we carried out normal-state Hall-effect measurements at 2 K for different V_G values. The deduced carrier density n_S and Hall mobility μ are summarized in Fig. S6b. The Hall mobility decreases from ~134.0 to ~113.8 cm^2/Vs as V_G changes from +150 V to –100 V, while the carrier density decreases from ~3.8×10^{13} to ~2.9×10^{13} cm^{-2}. Using n_S and R_S values in Figs. S6a and S6b, we calculated the mean free path l_{mfp} as a function of V_G, as shown in Fig. S6c. As V_G decreases from +150 to −100 V, the l_{mfp} decreases from 13.7 to 10.2 nm. The application of a negative V_G will push charge carriers towards the a-CZO/KTO(111) interface, leading to a higher degree of disorder and, consequently, an increase of resistance, as indicated by the increase in normal-state sheet resistance $R_{1.2K}$. Fig. S6c also plots the peak resistance ΔR_S as a function of V_G. Notably, ΔR_S decreases from 13.4 to 9.8 Ω/□ as V_G changes from +150 V to –100 V. This reduction in ΔR_S cannot be explained by enhanced disorder, as the higher disorder induced by negative V_G generally results in an increased resistance. The decrease in ΔR_S as V_G decreases could be attributed to reduced carrier density, which results in more sparsely distributed superconducting islands in a non-superconducting background. Consequently, the resistance effect induced by vortex motion across the weak links between superconducting grains is weakened.

To explore the dependence of H_{C2} on n_S, the sheet resistance as a function of magnetic field at 0.05 K for various back gate voltages is shown in Figs. S6d and S6e under out-of-plane and in-plane magnetic fields, respectively. The dependence of $\mu_0H_{C2\perp}$, $\mu_0H_{C2\parallel}$ and $\mu_0H_{C2}^{P}$ on V_G is shown in Fig. S6f, where $\mu_0H_{C2}^{P}$ is calculated using the values of T_C for different V_G. The much higher $\mu_0 H_{C2||}$ relative to $\mu_0 H_{C2}^{P}$ is observed. Based on the dependence of carrier density n_S on V_G at 2 K (Fig. S6b), the $\mu_0 H_{C2||}$ is plotted as a function of n_S in Fig. S6g, and $\mu_0 H_{C2||}$ increase from 3.6 to 5.0 T as n_S decreases from 3.8×10^{13} cm^{-2} to 2.9×10^{13} cm^{-2}. Note that a higher $\mu_0 H_{C2||}$ is observed in the a-CZO/KTO(111) system compared to LAO/STO (111) systems (~4.5 T)[1].

For a 2D superconductor with strong spin-orbit interaction, the in-plane upper critical field $\mu_0 H_{C2||}(0)$ can be expressed as[1,2]:

$$\mu_0 H_{c2||}(T=0) = \sqrt{\frac{1.76\hbar k_B T_C}{[3\mu_B^2 \tau_{so} + D(d_{sc} e)^2/3]}} \tag{S1}$$

where τ_{so} is the spin-orbit scattering lifetime, with spin-orbit energy $\varepsilon_{so}=\hbar/\tau_{so}$, D is the diffusion constant, and d_{sc} is the superconductive layer thickness. The diffusion constant D can be obtained from the slope of the out-of-plane upper critical field: $[-d(\mu_0\mu_0 H_{C2\perp})/dT]_{T=T_C} = 4k_B/\pi De$, and $D=9.6\times10^{-4}$ J/CT for sample with $n_S=3.8\times10^{13}$ cm^{-2} by fitting the data shown in Fig. 2c. Based on Ginzburg-Landau theory, we can track the evolution of ξ_{GL} and d_{SC} as a function of n_S (Fig. S6h). Adopting the T_C values under different V_G (Fig. S6a), we can obtain the n_S-dependent ε_{so} as plotted in Fig. S6i, revealing a tunability of the SOC at the a-CZO/KTO(111) interface. Obviously, ε_{so} increases as n_S decreases, consistent with the variation of $\mu_0 H_{C2||}$ with n_S. Based on the above analysis, the origin of the $\mu_0 H_{C2||}$ value exceeding the Pauli limit could be attributed to the strong spin-orbit coupling of the 5*d* 2DEG at KTO-based interfaces.

Note 2: Phase-slip model dependence on superconducting critical current and sweep rate

The peak resistance ΔR_S due to vortex motion, driven by thermally activated phase slips (TAPS), follows the form[3]:

$$\Delta R_S = A\dot{B}e^{-\alpha Ic/k_B T} \tag{S2}$$

where A and α are numerical constants at a fixed temperature, $\dot{B}$ is the magnetic field sweep rate, and I_c is the superconducting critical current.

(i) Dependence of peak resistance on critical current

We systematically investigated the effects of field-effect gating for the a-CZO/KTO(111) sample with $n_S=3.8\times10^{13}$ cm^{-2}, which corresponds to the n_S value of the as-grown sample. Fig. 3b shows the evolution of in-plane magnetoresistance with different V_G at 0.05 K under the field sweep rate of 0.10 T/min. It is found that ΔR_S decreases from 13.4 to 9.8 Ω/□ as V_G changes from +150 V to –100 V. As shown in Fig. S15a, I_C can also be tuned by changing the gate voltage V_G at 0.05 K. The inset shows the dependence of I_c on V_G. According to Equation S2, the relationship between ln(ΔR_S) and the critical current I_c is expected to be linear. Fig. S15b shows the dependence of ln(ΔR_S) on I_c, where a linear dependence is indeed observed. Based on the linear fit (solid line), the fitting parameters A =2828×10^5 Ωmin/□T and the exponential factor α/k_BT= 1.8×10^5 A^{-1}.

(ii) Dependence of peak resistance on magnetic field sweep rate

As shown in Fig. 3c, the magnitude of the MR curve strongly depends on the field sweep rate at T=0.05 K for the a-CZO/KTO(111) sample with n_S=4.3×10^{13} cm^{-2}. In Fig. S15c, ΔR_S is plotted as a function of the magnetic field sweep rate, using data extracted from Fig. 3c. According to Eq. S2, ΔR_S is proportional to the magnetic field sweep rate. The solid line in Fig. S15c represents a linear fit, with a slope of 254 Ωmin/□T.

Table S1. The fitted result represents the binding energy and composition proportion of Ta^{5+} and Ta^{4+}.

Ta^{x+}	Orbital	Binding Energy (eV)	Amounts of Ta^{x+} (%)
Ta^{5+}	Ta $4f_{5/2}$	28.14	77.2
	Ta $4f_{7/2}$	26.22	
Ta^{4+}	Ta $4f_{5/2}$	24.83	22.8
	Ta $4f_{7/2}$	22.88	

Table S2. Summary of sample properties including the substrate temperature during growth (T_S), the oxygen pressure (P_{O2}), carrier density n_S and Hall mobility (μ).

Sample	T_S (°C)	P_{O2} (Pa)	n_S (cm^{-2}) T=10 K	μ(cm^2/Vs) T=10 K
#1	300	5×10^{-3}	3.8×10^{13}	120
#2	300	1×10^{-3}	4.3×10^{13}	395
#3	300	1×10^{-4}	5.8×10^{13}	68
#4	300	3×10^{-5}	8.9×10^{13}	16
#5	300	1×10^{-5}	9.8×10^{13}	68

Table S3. Summary of studies on magnetotransport properties in the superconducting state of KTO(111) heterostructures, where "√" denotes that MR measurements were conducted and "×" indicates that no MR measurements were performed. Note that MR loop behavior is observed in low-n_S a-CZO/KTO(111) samples under in-plane magnetic fields.

Year	Author	Heterostructures	n_S (10^{13} cm^{-2})	Superconducting state MR measurements	
				In-plane	Out-of-plane
This work	Zhang H, *et al.*	a-CZO/KTO(111)	3.8 to 9.8 at 10 K	√	√
2021	Liu C, *et al.*[4]	EuO/KTO(111)	3.5 to 9.9 at 10 K	×	√
			9.2 at 10 K	√	√
		a-LAO/KTO(111)	8.9 at 10 K	√	√
2023	Zhang G, *et al.*[5]	$YAlO_3$/KTO(111)	6.6 at 5 K	×	√
			14.5 at 5 K	√	√
			31.0 at 5 K	√	×
2023	Liu Y, *et al.*[6]	$LaVO_3$/KTO(111)	14.0 at 2 K	√	√
2023	Arnault E, *et al.*[7]	$LaSrMnO_3$/KTO(111)	6.0 at 3 K	√	√

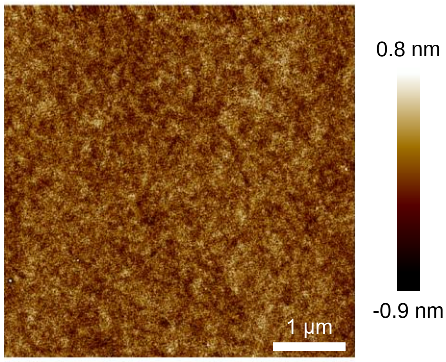

Figure S1. Atomic force microscope (AFM) image of a-CZO films (10 nm) grown on the KTO(111) substrate. The size in AFM image is 5×5 μm^2. The film is very flat with a root-mean-squared roughness of 0.19 nm.

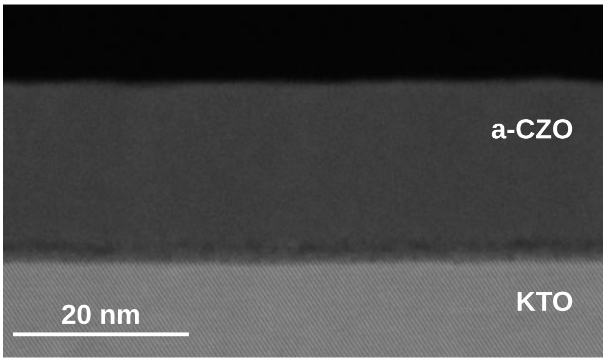

Figure S2. A large-scale HAADF-STEM image of the a-CZO(20 nm)/KTO(111) heterostructure, measured along [1-10] zone axis.

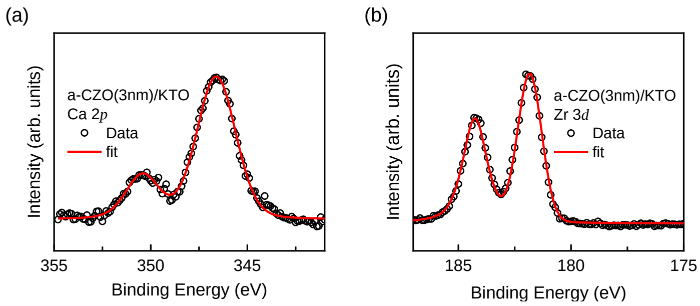

Figure S3. X-ray photoelectron spectra results of (a) Ca, (b) Zr and (c) Ta for the a-CZO(3nm)/KTO(111) sample. The fitted peaks for Ta^{5+} and $Ta^{4+}$are shown in blue and green colors, respectively. The data and sum fit envelope are shown in black circles and red lines.

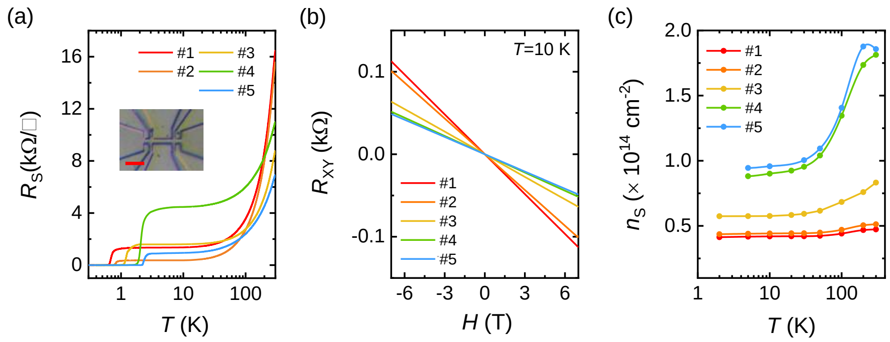

Figure S4. (a) Temperature dependence of sheet resistance. Inset: Photograph of the fabricated Hall-bar device. The central Hall bar bridge is 20 μm in width and 120 μm in length. The red scale bar represents 100 μm. (b) Hall resistance as a function of magnetic field at T=10 K for 2DEGs formed at the a-CZO/KTO(111) interface in series of samples prepared at different growth conditions. (c) Temperature dependence of carrier density n_S. Numbers in the figures denote different samples.

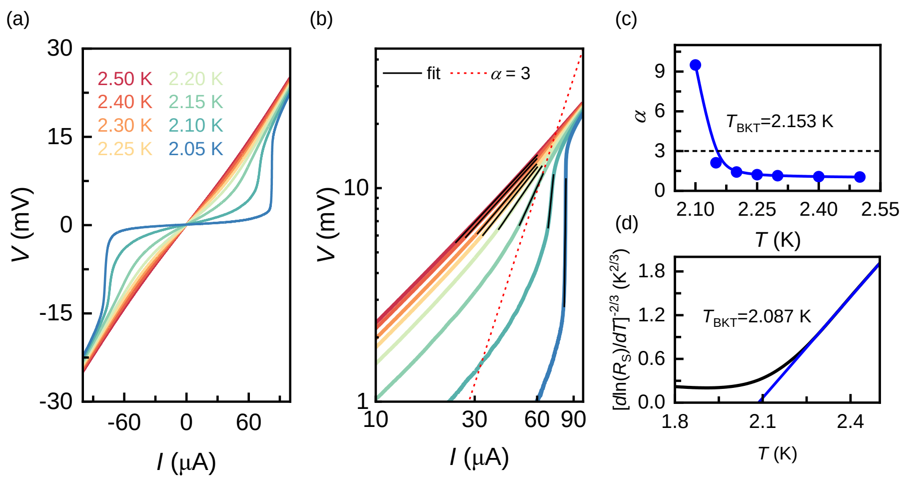

Figure S5. (a) Temperature-dependent *I*-*V* measurements for sample with n_S=9.8×10^{13} cm^{-2}. (b) *I*-*V* curves plotted on a logarithmic scale with the same color codes as in (a). Red dashed line represents $V \propto I^3$, which is used to infer the BKT transition temperature. (c) Temperature dependence of the power-law exponent α, as deduced from the linear fits of the curves in (b). T_{BKT}=2.153 K is obtained. (d) Sheet resistance dependence of temperature plotted on a $[d\ln(R_S)/dT]^{-2/3}$ scale. The blue solid line is a linear extrapolation from the high-*T* linear section, which crosses the *T*-axis at T_{BKT}=2.087 K.

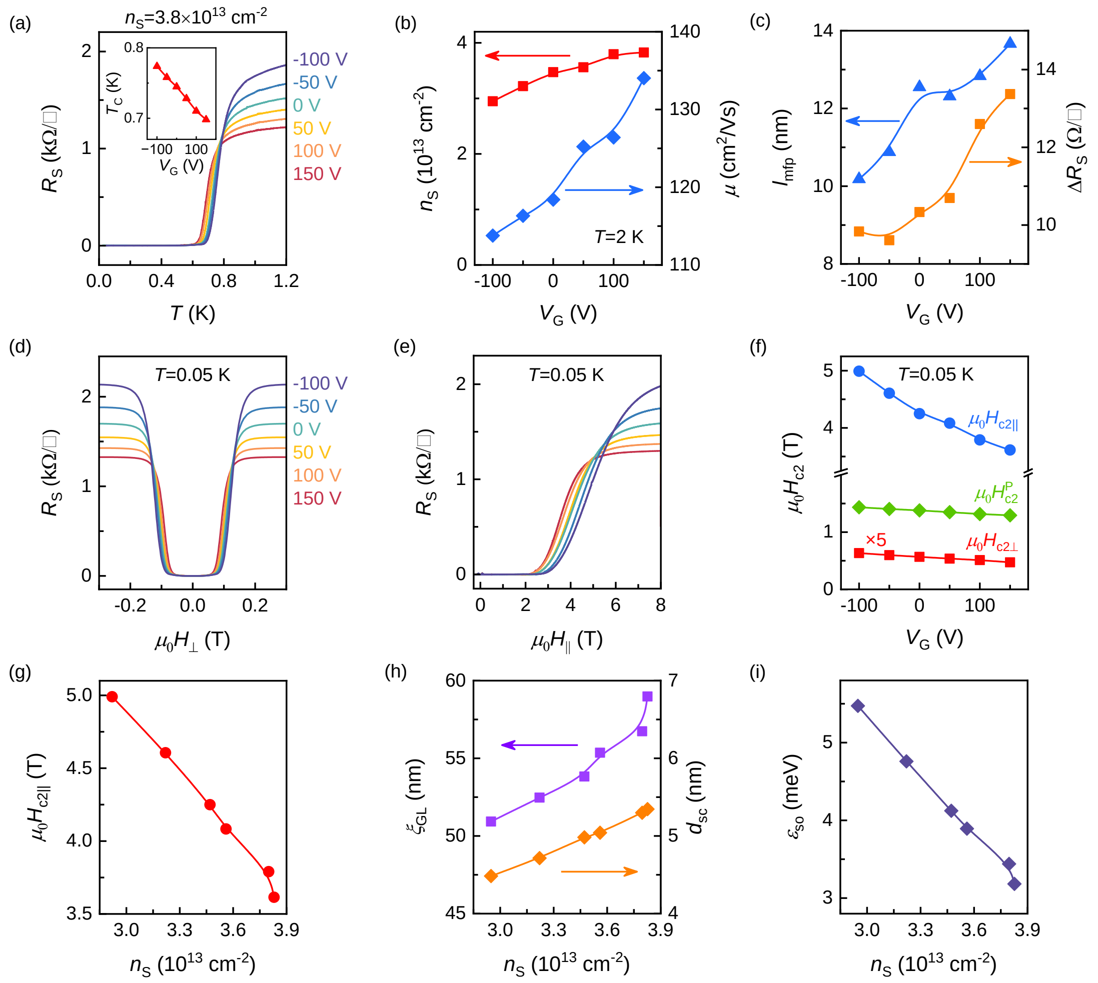

Figure S6. (a) Temperature dependent R_S at different V_G values for the a-CZO/KTO(111) sample with n_S=3.8×10^{13} cm^{-2}, which corresponds to the n_S value of the as-grown sample. Inset: midpoint T_C plotted as a function of V_G. (b) Carrier density n_S and Hall mobility μ as a function of V_G measured at 2 K. (c) Mean free path l_{mfp} and peak resistance ΔR_S as a function of V_G. Magnetoresistance R_S at 0.05 K in (d) out-of-plane and (e) in-plane magnetic field at different V_G. (f) The dependence of upper critical field $\mu_0 H_{C2\perp}$, $\mu_0 H_{C2\parallel}$ and $\mu_0 H_{c2}^{P}$ on V_G. (g) In-plane upper critical field $\mu_0 H_{C2\parallel}$, (h) coherence length ξ_{GL} and superconducting layer thickness d_{SC}, and (i) spin-orbit energy ε_{SO} as a function of n_S.

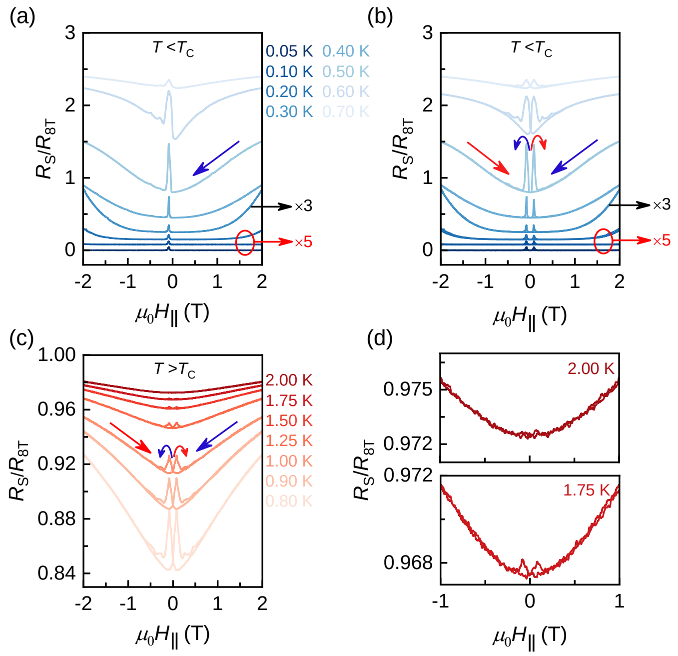

Figure S7. (a) Temperature-dependent in-plane MR loops for the a-CZO/KTO(111) sample with n_S=3.8×10^{13} cm^{-2} and T_C=0.67 K in the superconducting state (T<T_C). (b) Temperature-dependent in-plane MR loops for two sweep directions, where twin peaks have appeared in the superconducting state (T<T_C). Data obtained at different temperatures were shifted vertically for clarity. (c) Temperature-dependent in-plane MR loops for the a-CZO/KTO(111) sample with n_S=3.8×10^{13} cm^{-2} and T_C=0.67 K in the normal state (T>T_C). (d) A magnified view of the MR loops, obtained at 1.75 K and 2 K.

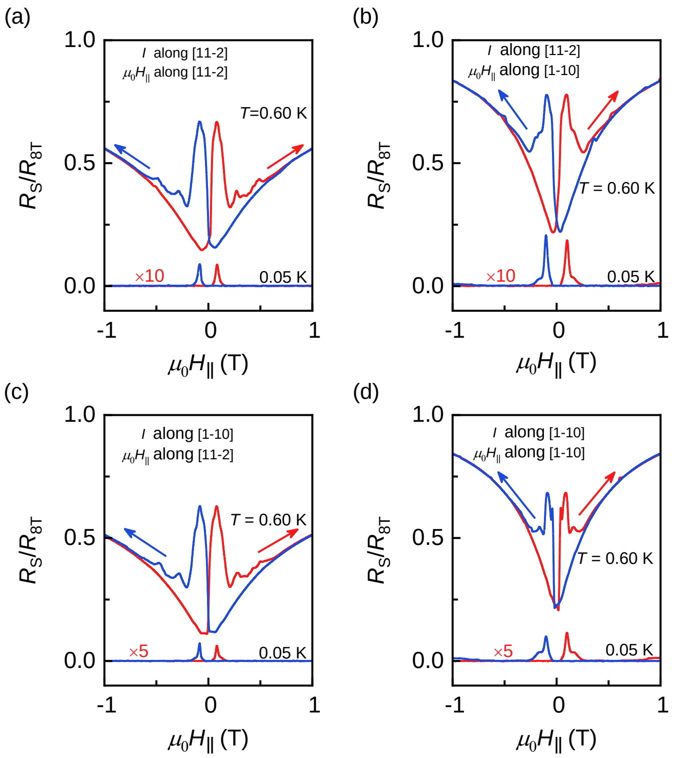

Figure S8. R_S/R_{8T} as a function of the in-plane magnetic field when (a) I along [11-2] with $\mu_0H_{\|}$ along [11-2] (b) I along [11-2] with $\mu_0H_{\|}$ along [1-10], (c) I along [1-10] with $\mu_0H_{\|}$ along [11-2] and (d) I along [1-10] with $\mu_0H_{\|}$ along [1-10]. In all cases, hysteresis appears, indicating that the direction of I and $\mu_0H_{\|}$ are not the significant factors on the peaks.

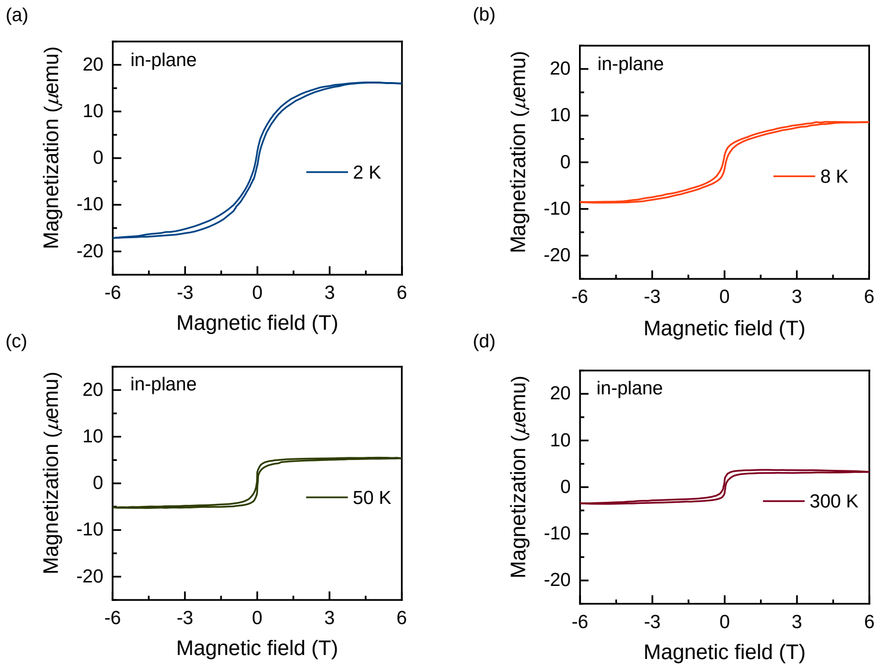

Figure S9. Magnetic field-dependent magnetizations at various temperatures with in-plane field for the a-CZO/KTO(111) sample with n_S=3.8×10^{13} cm^{-2}.

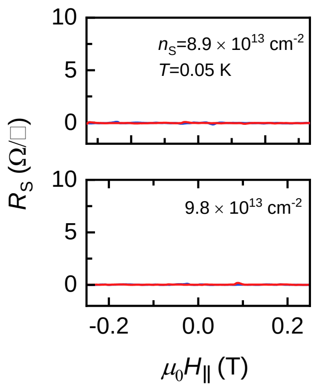

Figure S10. In-plane magnetoresistance for samples with n_S=8.9×10^{13} cm^{-2} and 9.8×10^{13} cm^{-2} at 0.05 K, where hysteresis loop is invisible.

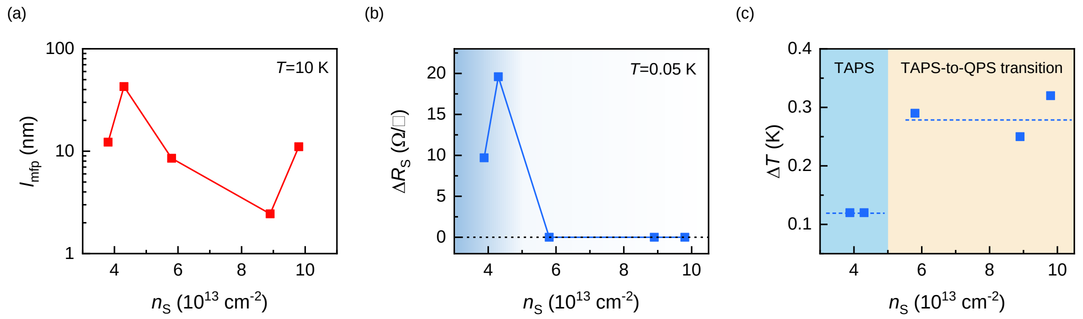

Figure S11. (a) The mean free path l_{mfp} is plotted a function of n_S, which ranges from 3.8×10^{13} to 9.8×10^{13} cm^{-2}. (b) Peak resistance ΔR_S at 0.05 K as a function of n_S. (c) Dependence of the superconducting transition width ΔT on n_S.

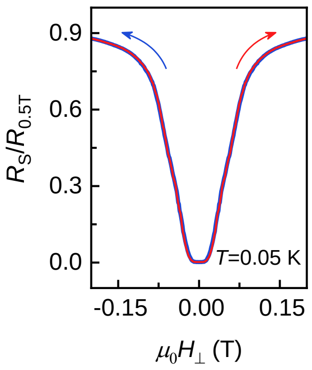

Figure S12. Out-of-plane magnetoresistance for samples with n_S=3.8×10^{13} cm^{-2} at 0.05 K for two sweep direction, where butterfly shaped hysteresis is absent.

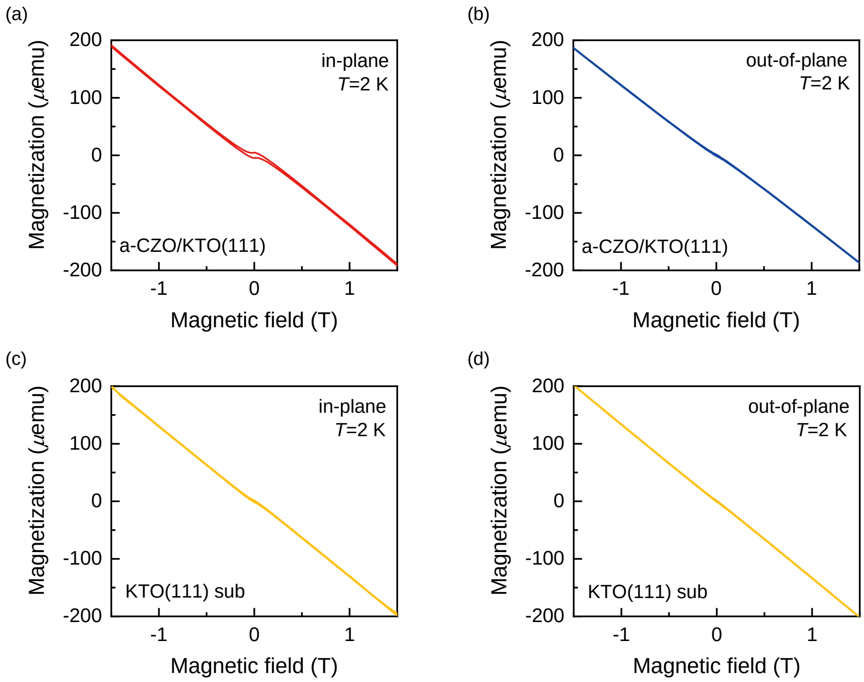

Figure S13. (a) In-plane and (b) out-of-plane magnetizations at 2 K for the a-CZO/KTO(111) sample with n_S=3.8×10^{13} cm^{-2}. (c) In-plane and (d) out-of-plane magnetizations at 2 K for the bare KTO(111) substrate.

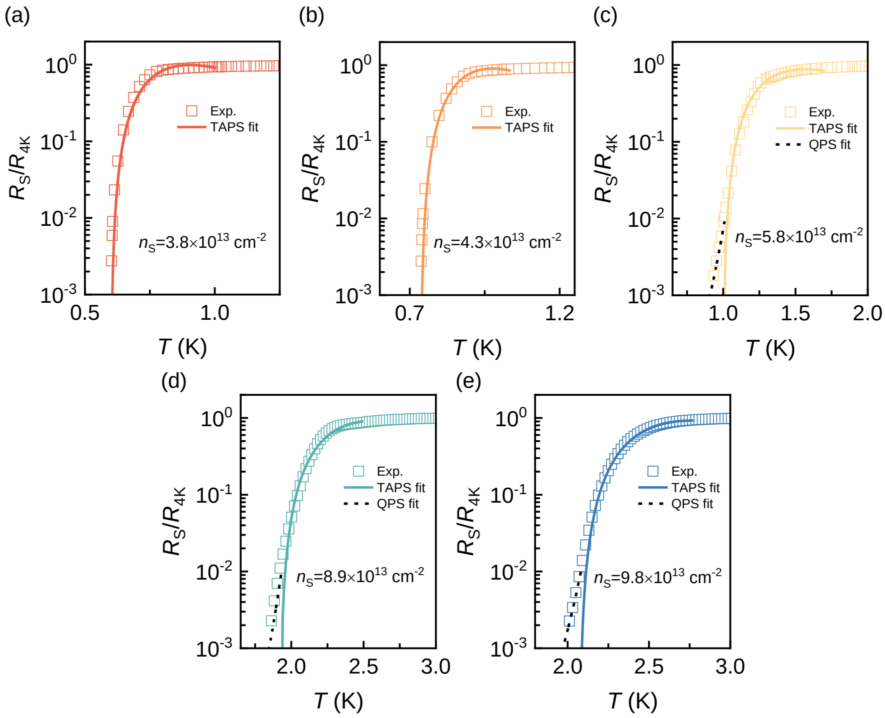

Figure S14. (a)-(e) R_S/R_{4K} as a function of normalized temperature T-T_C for samples with carrier density ranging from 3.8×10^{13} to 9.8×10^{13} cm^{-2}. The marks represent the experimental data. The solid lines and dashed black lines are fitting curves using the LAMH theory for the TAPS model and the Golubev-Zaikin theory for the QPS model, respectively. The hollow patterns indicate the values of carrier densities.

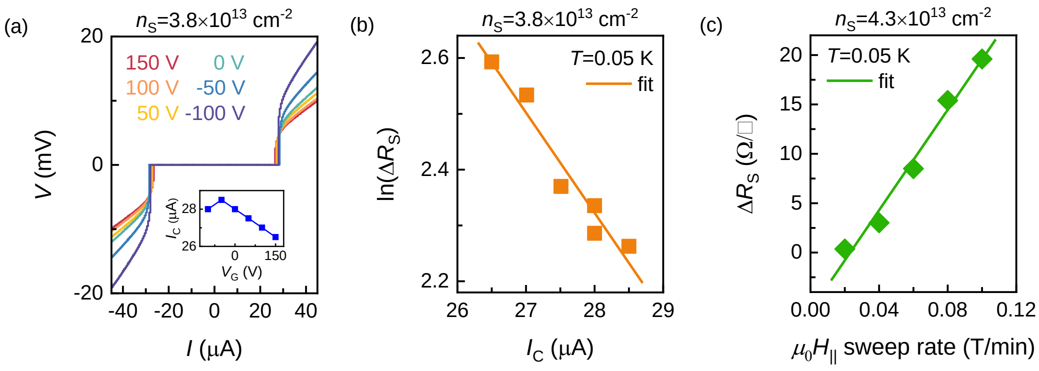

Figure S15. (a) *I-V* measurement for different V_G at $T = 0.05$ K for the a-CZO/KTO(111) sample with n_S=3.8×10^{13} cm^{-2}, which corresponds to the n_S value of the as-grown sample. Inset shows the dependence of *I*c on V_G. (b) The dependence of ln(ΔR_S) on *I*c for the same sample in (a). (c) ΔR_S as a function of the in-plane field sweep rate for the a-CZO/KTO(111) sample with n_S=4.3×10^{13} cm^{-2} at T=0.05 K obtained from the data in Fig. 3c.

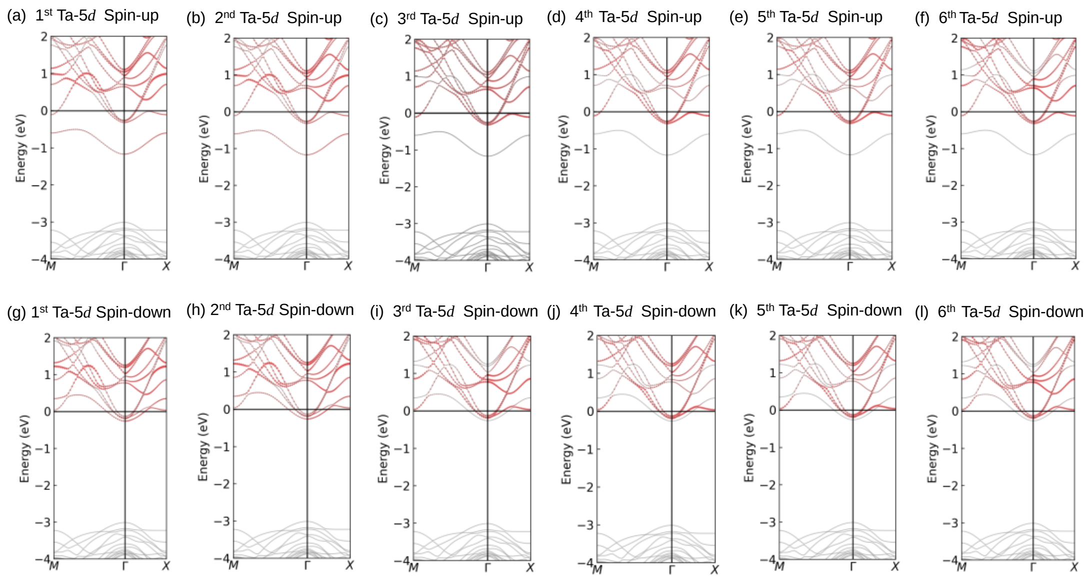

Figure S16. Calculated atom-resolved and layer-dependent band structure for Ta 5*d* orbitals from the first to the sixth Ta atomic layer in (a-f) spin-up and (g-l) spin-down states.

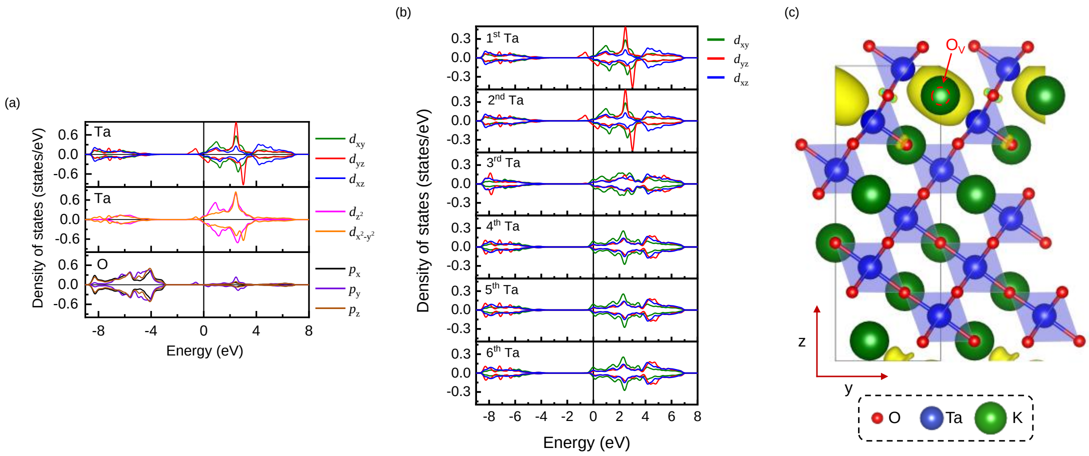

Figure S17. (a) The orbital-resolved density of states for the Ta atoms and oxygen atoms around the oxygen vacancy. (b) Partial density of states projected on *d* orbitals from Ta atoms for KTO(111) layer with an oxygen vacancy. The Fermi levels are all set to zero and indicated by black lines. (c) The real-space spin density $\Delta\rho=\rho_{\uparrow}-\rho_{\downarrow}$ of the KTO(111) layer with one vacancy. The black box represents the unit cell used in the calculation. The spin-density isosurface is represented in yellow, with an isovalue set at 0.0027 eV/Å^3.

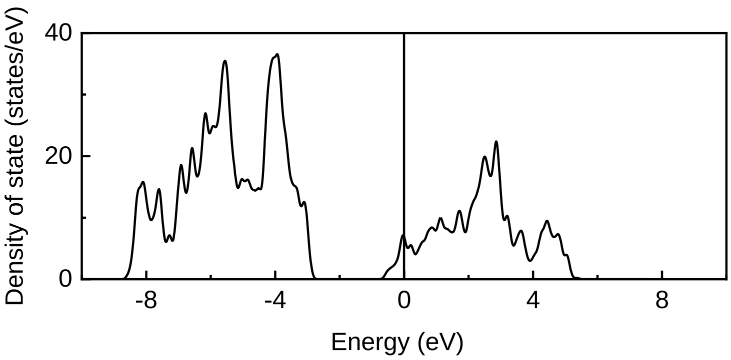

Figure S18. The total non-spin-polarized density of states of KTO(111) layer with an oxygen vacancy.

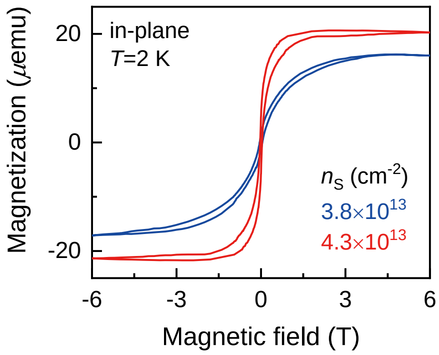

Figure S19. Magnetic field-dependent magnetizations at 2 K with in-plane field for the a-CZO/KTO(111) samples with different n_S.

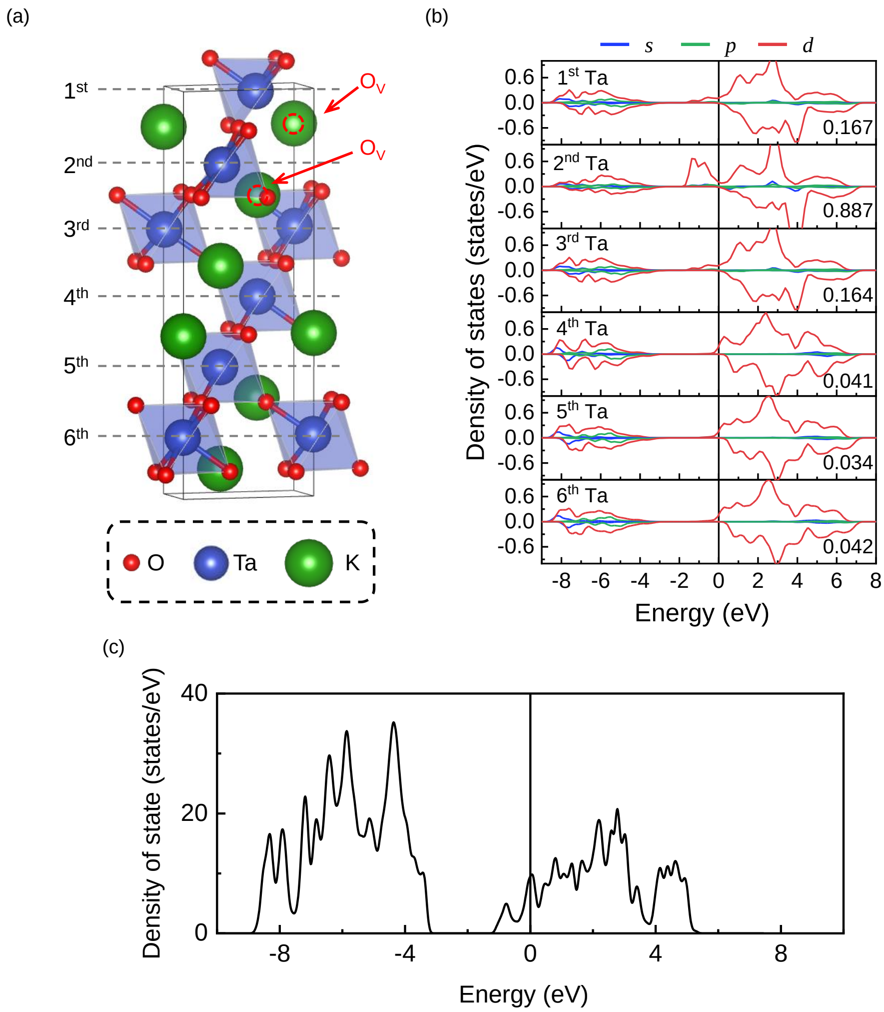

Figure S20. (a) Structural model of the KTO(111) layer with two oxygen vacancies for DFT calculation. (b) The orbital-resolved and layer-dependent density of states for the Ta atoms. (c) The total non-spin-polarized density of states of KTO(111) layer with two oxygen vacancies.

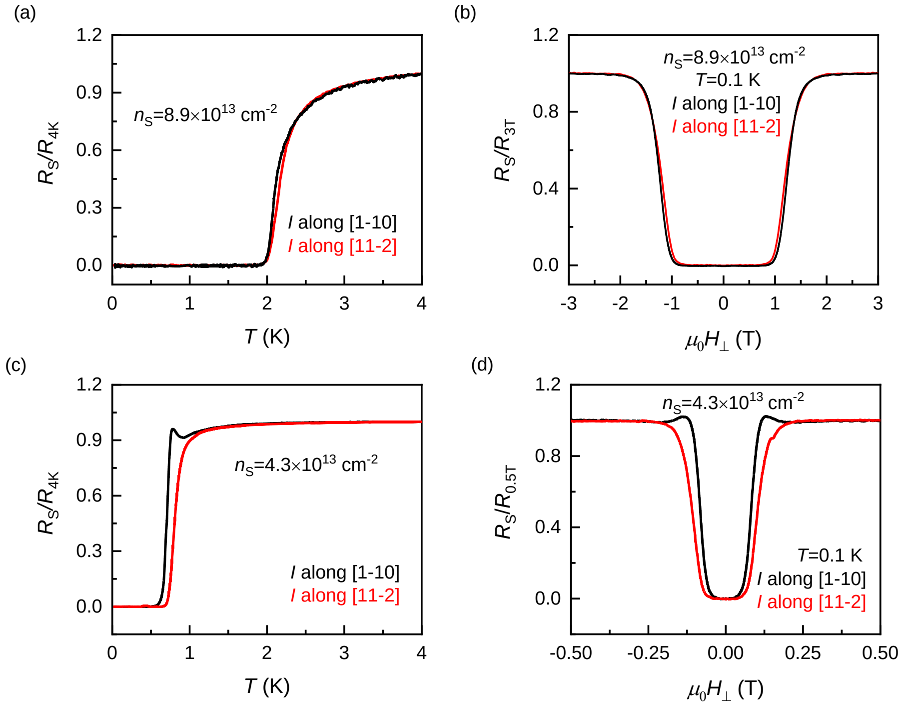

Figure S21. (a) R_S/R_{4K} as a function of temperature for the a-CZO/KTO(111) sample with n_S=8.9×10^{13} cm^{-2}. (b) Normalized out-of-plane MR measured at T=0.1 K for the same sample. Black and red curves represent current along [1-10] and [11-2], respectively. (c) Temperature-dependent R_S/R_{4K} and (d) normalized out-of-plane MR measured at T=0.1 K for a-CZO/KTO(111) samples with n_S=4.3×10^{13} cm^{-2}. Black and red curves represent current along [1-10] and [11-2], respectively.

References

1. Rout P, Maniv E, Dagan Y. Link between the superconducting dome and spin-orbit interaction in the (111) $LaAlO_3/SrTiO_3$ interface. Physical review letters 119, 237002 (2017).
2. Hua X, et al. Tunable two-dimensional superconductivity and spin-orbit coupling at the $EuO/KTaO_3$(110) interface. npj Quantum Materials 7, 97 (2022).
3. Mehta M, et al. Evidence for charge–vortex duality at the $LaAlO_3/SrTiO_3$ interface. Nature Communications 3, 955 (2012).
4. Liu C, et al. Two-dimensional superconductivity and anisotropic transport at $KTaO_3$(111) interfaces. Science 371, 716-721 (2021).
5. Zhang G, et al. Spontaneous rotational symmetry breaking in $KTaO_3$ heterointerface superconductors. Nature Communications 14, 3046 (2023).
6. Liu Y, Liu Z, Zhang M, Sun Y, Tian H, Xie Y. Superconductivity in epitaxially grown $LaVO_3/KTaO_3$ (111) heterostructures. Chinese Physics B 32, 037305 (2023).
7. Arnault EG, et al. Anisotropic superconductivity at $KTaO_3$ (111) interfaces. Science Advances 9, eadf1414 (2023).